Electronic Supplementary Material (ESI) for Journal of Materials Chemistry A.

Enhancing interfacial charge transfer in $WO_3/BiVO_4$ photoanode heterojunction through gallium and tungsten co-doping and sulfur modified Bi_2O_3 interfacial layer

Umesh Prasad[1,2], James L. Young[2]*, Justin C. Johnson[2], Deborah L. McGott[2,3], Hengfei Gu[4], Eric Garfunkel[4] and Arunachala M. Kannan[1]*

[1]The Polytechnic School, Ira A. Fulton Schools of Engineering, Arizona State University, Mesa, AZ 85212, USA

[2]National Renewable Energy Laboratory, Golden, CO 80401, USA

[3]Colorado School of Mines, Golden, CO, 80401, USA

[4]Department of Chemistry and Chemical Biology, Rutgers University, Piscataway, NJ 08854, USA

*Corresponding Author: Email amk@asu.edu, james.young@nrel.gov

Section 1: Calculation processes

Photoelectrochemical measurements

The reference electrode potential was converted to reverse hydrogen electrode (RHE) by the relationship given in (equation (1)).

$$E_{RHE} = E_{Ag/AgCl}{}^{0} + E_{Ag/AgClSCE} + 0.059\,pH \quad (1)$$

$$Where\ \ E_{Ag/AgCl}{}^{0} = 0.1976\,V\ vs.RHE, at\ 298\,K$$

Process of theoretical photocurrent ($J_{theoretical}$ calculation)

The light-harvesting efficiency (LHE) or absorption efficiency (ϕ_{abs}) relationship is show in (equation (2))

$$LHE = 1 - 10^{-A(\lambda)} \quad = \phi_{abs} \quad (2)$$

Where A is absorbance with wavelength (λ)

The absorption efficiency was calculated by integrating absorption spectra from wavelength 300 to 550 nm for all samples.

Further, photon energy and photon flux calculated from AM1.5G solar irradiance with wavelength as given in Figure S1b by following relation (equation (3-5)).

$$E(\lambda) = h \times C/\lambda \quad (3)$$

$$Where, E(\lambda): photon\ energy \quad h: Plank\ constant \quad C: speed\ of\ the\ light$$

$$Number\ of\ photons = h \times C/\lambda \quad (4)$$

$$Photons\ flux\ (\phi(\lambda)) = P(\lambda)/E(\lambda) \quad (5)$$

The above-calculated data, theoretical photocurrent was calculated assuming 100% incident to photon conversion efficiency (IPCE) and by the following relationship.[1,2]

$$J_{theoretical} = \int_{\lambda_1}^{\lambda_2} e \times \phi(\lambda) \times LHE \times d\lambda \qquad (6)$$

Charge transport calculation: bulk and surface

Major losses in theoretical photocurrent are electron-hole recombination in the bulk and at the surface, which are known as charge separation (ϕ_{sep}) and charge transfer or charge injection efficiency (ϕ_{trans}), by relationship equation (7 and 8).

$$J_{H_2O} = J_{theoretical} \times \phi_{sep} \times \phi_{trans} \qquad (7)$$

The transfer efficiency is almost 100% in the presence of hole scavengers, given by relationship equation (10).[2]

$$J_{Na_2SO_3} = J_{theoretical} \times \phi_{sep} \qquad (8)$$

Using equation (7 and 8) the ϕ_{sep} and ϕ_{trans} can be calculated

IPCE calculation

The IPCE was measured by the relationship given in equation (9)

$$IPCE = \frac{Number\ of\ electrons}{Number\ of\ photons} = \frac{J_{monochromator} \times h \times C}{P_{monochromator} \times \lambda} \qquad (9)$$

Integrated current calculation

Integrated current ($J_{integrated}$) was calculated using the relationship given in eq (10)

$$J_{Integrated} = \int_{\lambda_1}^{\lambda_2} e \times \phi(\lambda) \times IPCE \times LHE \times d\lambda \qquad (10)$$

Section 2: Photocurrent measurements and fabrication steps

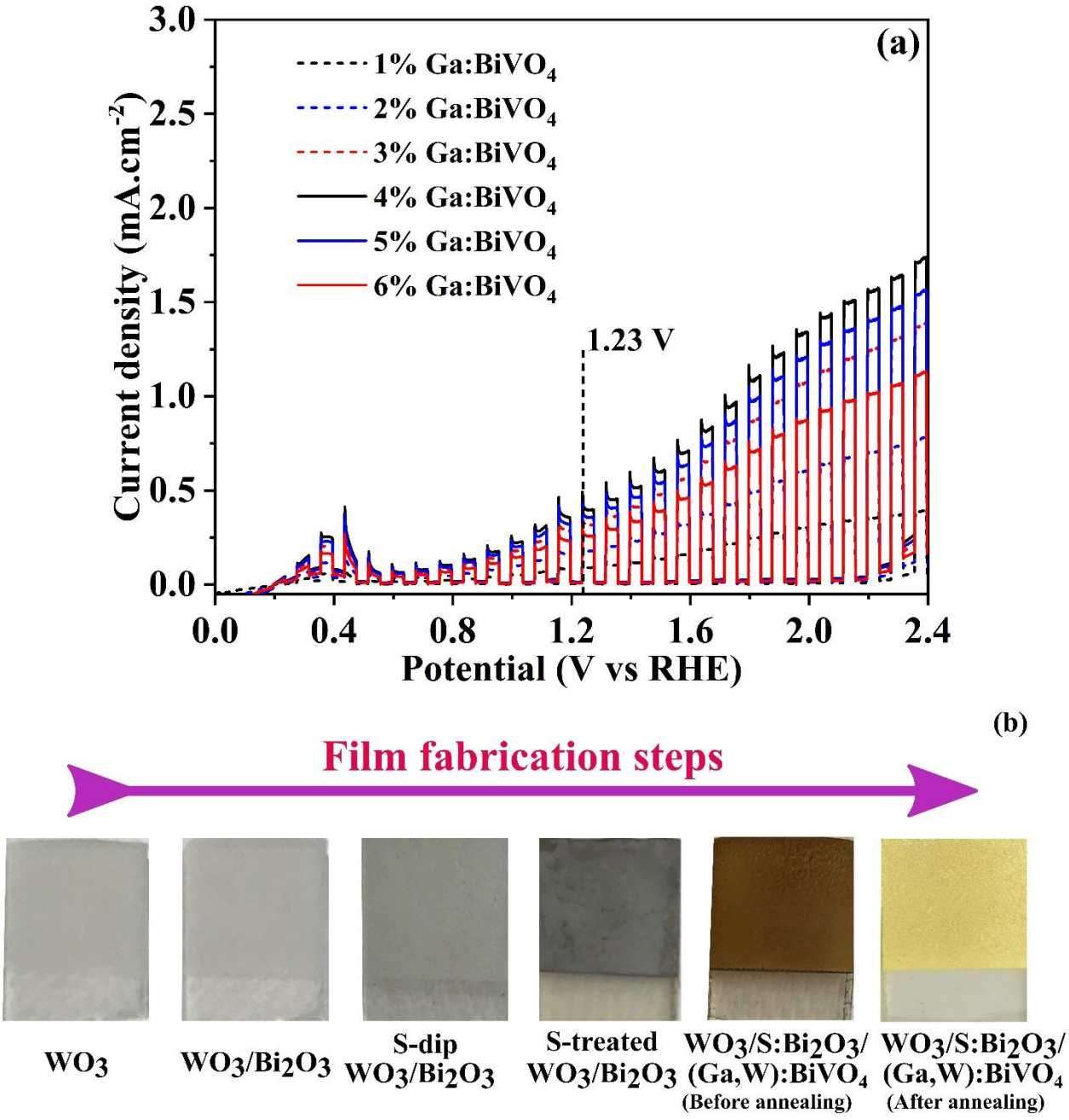

Figure S1. Chopped light J-V plot for 1- 6 wt % Ga-doped $BiVO_4$ in KPi electrolyte. (b) Fabrication steps of WO_3/S:Bi_2O_3/(Ga,W):$BiVO_4$ sample.

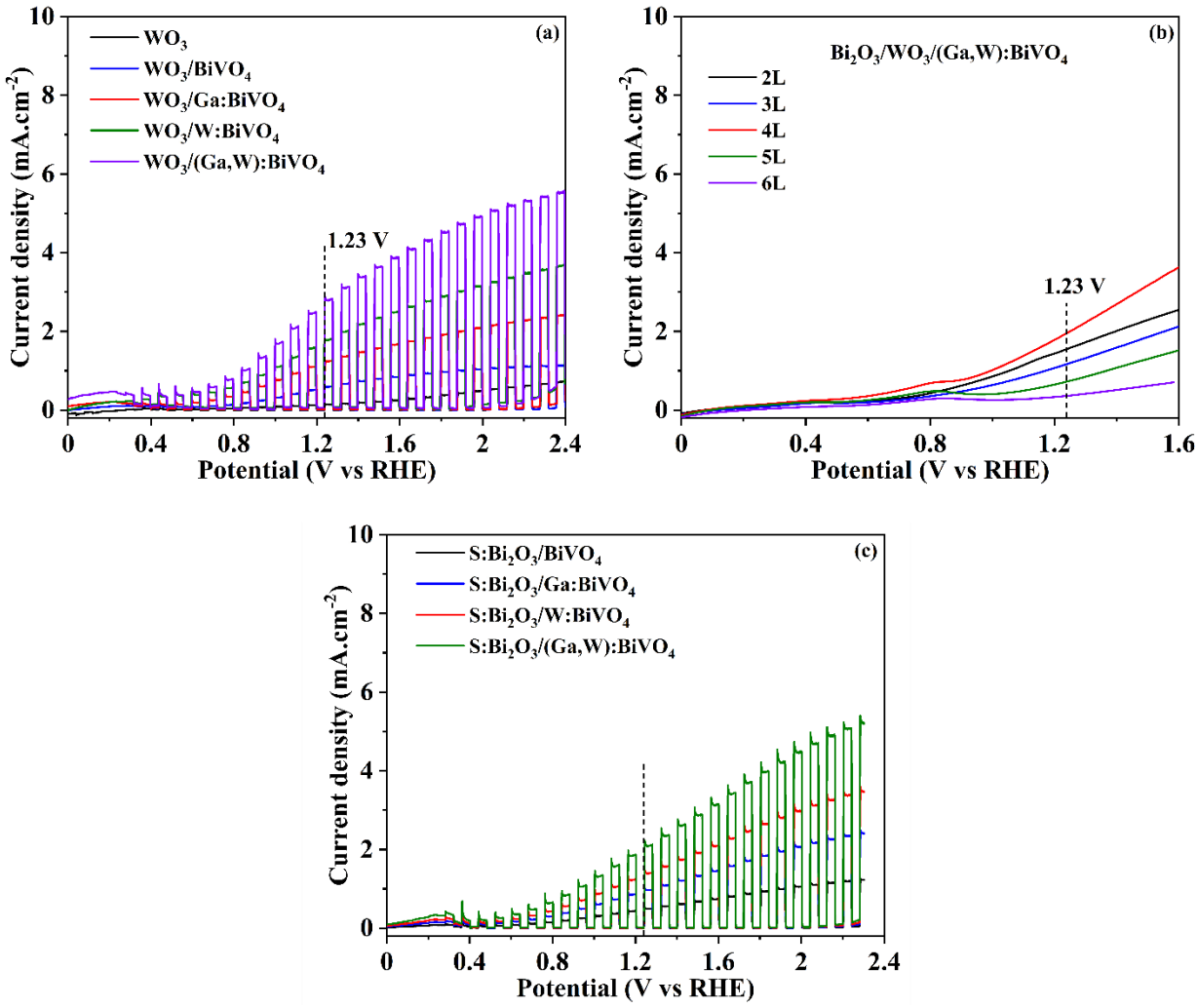

Figure S2. J−V plots under simulated AM 1.5G illumination in KPi for (a) WO_3/doped $BiVO_4$ photoanodes, (b) different layers of Bi_2O_3 with WO_3/doped $BiVO_4$, (c) heterojunction between S:Bi_2O_3 and doped $BiVO_4$.

Section 3: Photocurrent measurements of hole scavengers

The photocurrent was also measured with a hole scavenger (Na_2SO_3), where the electron-hole recombination is considered almost negligible.1

[1] As observed from Figure S3, WO_3/S:Bi_2O_3/(Ga,W):$BiVO_4$ exhibited the highest photocurrent of 6.4±0.3 mA.cm^{-2} compared to 5.86±0.3 and 5.4±0.28 mA.cm^{-2} for WO_3/Bi_2O_3/(Ga,W):$BiVO_4$ and

WO_3/(Ga,W):$BiVO_4$ photoanodes, validating the significance of implementing an interfacial layer S:Bi_2O_3.

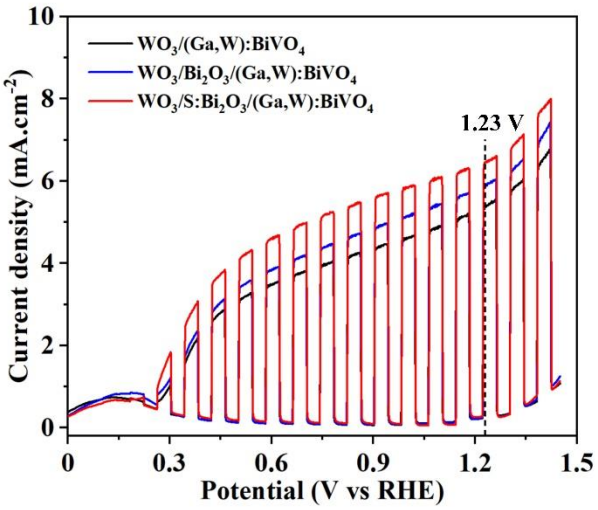

Figure S3. J–V plots under 1 sun illumination for photoanodes with WO_3 heterojunction and Bi_2O_3 interface layer with and without sulfur modification in KPi with hole scavenger (1M Na_2SO_3).

Section 4: Mott Schottky and flat-band calculation

Mott-Schottky estimated flat band (onset) potential–Schottky at 1 kHz in the dark with AC amplitude of 20 mV at 1.23 V vs RHE in 0.1 M K_2HPO_4 electrolyte (pH 7.5) by the relationship given in equation (12).[1]

$$\frac{1}{C^2} = \frac{2}{(\varepsilon\varepsilon_0 A^2 e N_D)} \left(V_{app} - V_{FB} - \frac{K_B T}{e}\right) \qquad (12)$$

Where C is the capacitance in space charge region; ε is relative permeability which is taken as[3] for the calculation; ε_0 is vacuum permeability (8.8×10^{-12} F m^{-1}); A (cm^2) is the area of the photoanode thin film; e is the charge of an electron (1.602×10^{-19} C); N_D is the number of charge carrier per cm^{-3}, estimated from Mott-Schottky measurement plot (Table S1); V_{app} (in RHE) is the applied potential; V_{FB} is the flat band potential measured from Mott-Schottky plot; K_B is

Boltzmann constant (1.38 × 10-23 J K^{-1}); T (K) is the temperature at which the measurement is performed (298 K).

Mott-Schottky measurements were performed in the frequency range of 0.7 – 2.8 kHz in the dark (Figure S4 a-d). Mott-Schottky measurements demonstrated the cathodic shift (Figure S4e) in the flat-band potential compared to the i-$BiVO_4$ that signified the reduced surface recombination.[3] The cathodic shifts in the flat-band potentials were 158, 202 and 209 mV, whereas corresponding shifts in the onset potentials for photocurrent were 380, 410 and 440 mV (Figure S4f) for WO_3/(Ga,W):$BiVO_4$, WO_3/Bi_2O_3/(Ga,W):$BiVO_4$ and WO_3/S:Bi_2O_3/(Ga,W):$BiVO_4$ photoanodes compared to i- $BiVO_4$. There were further 91 mV cathodic shift noticed on Co-Pi deposition for WO_3/S:Bi_2O_3/(Ga,W):$BiVO_4$/Co-Pi photoanodes. The slight difference in onset potential and flat-band potential could be due to the rate limitation in charge transfer to photoanode surface/electrolyte interface and recombination in space charge layer.[4] As shown in Figure S4e (inset), the shift in the CB edge for WO_3/S:Bi_2O_3/(Ga,W):$BiVO_4$ photoanode was much closer to the H_2 evolution potential (0 V_{RHE}), lessening the overpotential for driving hydrogen evolution reaction (HER) but increasing that available for driving the more difficult oxygen evolution reaction (OER), which provides a more favorable balance for the overall water splitting kinetics. The flat band was assumed to be equal to the CB edge, a good approximation for highly doped photoanodes.[5] The CB edge shift (Figure S4e: inset, Table S1) was more pronounced due to Ga and W co-doping and even more substantial with heterojunction formation and S modification.

The frequency dependency of the Mott-Schottky data was verified by conducting additional Mott-Schottky analysis at frequency values of 0.5, 1 and 2 kHz[4,6,7] in 0.1 M K_2HPO_4 electrolyte in the dark (see Figures S4 a-d) for i-$BiVO_4$, WO_3/(Ga,W):$BiVO_4$, WO_3/Bi_2O_3/(Ga,W):$BiVO_4$ and

WO_3/S:Bi_2O_3/(Ga,W):$BiVO_4$ photoanodes. As seen from these figures, the x-axis intercepts were close for all frequencies. The frequency dependency was also validated on real and imaginary impedance values. As seen from Figure S4 (g and h), the real impedance was unaffected with the change in frequency values, but the imaginary impedance showed log-log dependency with the slope value of -0.88±-0.15. High frequencies were selected in order to have a smaller time scale, which can abstain from the sufficient filled and vacant surface states or buildup of a double layer capacitance.[8]

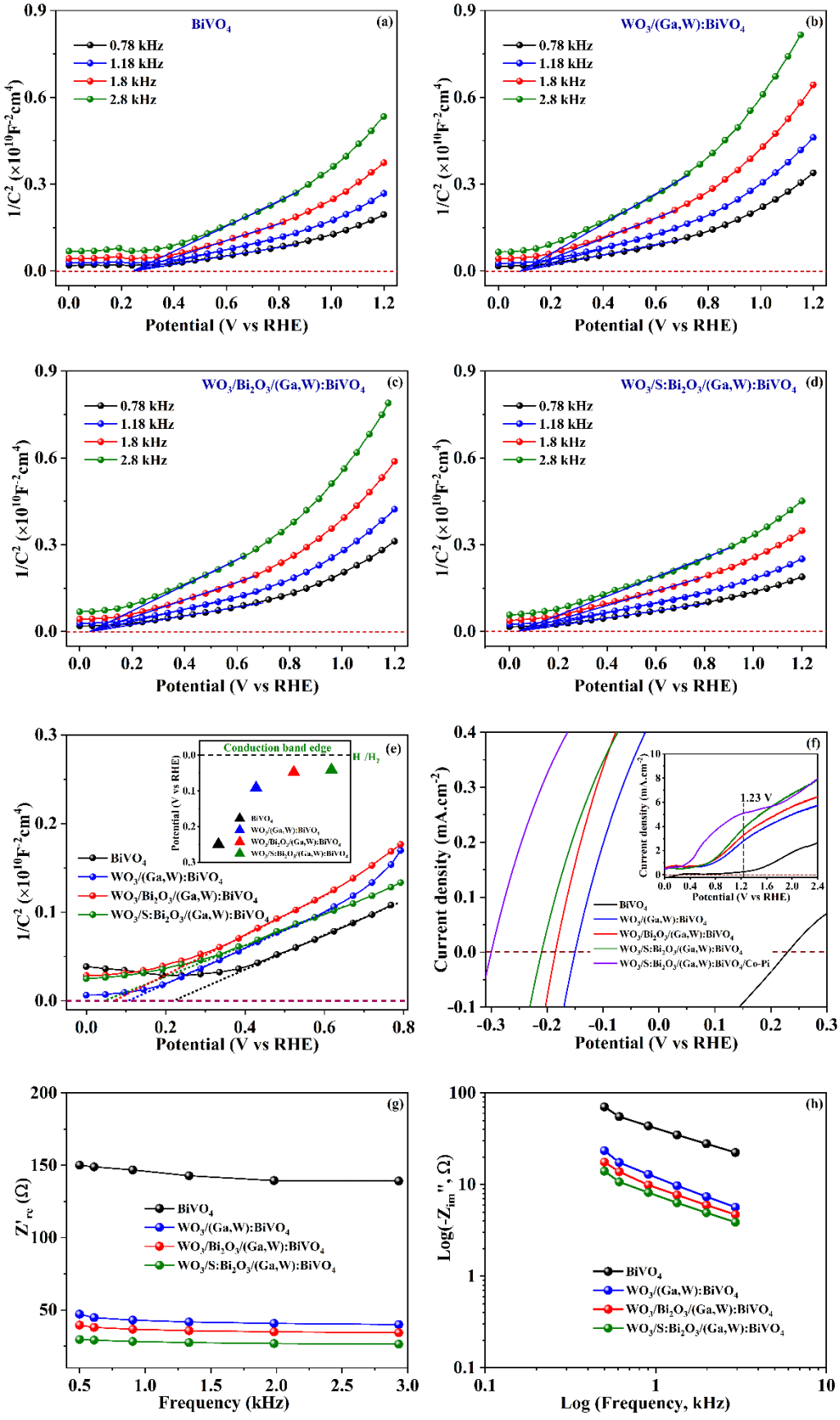
(a)
BiVO4
0.78 kHz
1.18 kHz
1.8 kHz
2.8 kHz
1/C2 (×10^10 F^-2 cm^4)
Potential (V vs RHE)
(b)
WO3/(Ga,W):BiVO4
(c)
WO3/Bi2O3/(Ga,W):BiVO4
(d)
WO3/S:Bi2O3/(Ga,W):BiVO4
(e)
Conduction band edge
H+/H2
Potential (V vs RHE)
BiVO4
WO3/(Ga,W):BiVO4
WO3/Bi2O3/(Ga,W):BiVO4
WO3/S:Bi2O3/(Ga,W):BiVO4
(f)
Current density (mA.cm-2)
1.23 V
Current density (mA.cm-2)
Potential (V vs RHE)
WO3/S:Bi2O3/(Ga,W):BiVO4/Co-Pi
(g)
Z're (Ω)
Frequency (kHz)
(h)
Log(-Zim'', Ω)
Log (Frequency, kHz)

Figure S4. Mott-Schottky analysis in KPi electrolyte measured in the dark at different frequencies of (a) $BiVO_4$, (b) WO_3/(Ga,W):$BiVO_4$ (c) WO_3/Bi_2O_3/(Ga,W):$BiVO_4$, and (d) WO_3/S:Bi_2O_3/(Ga,W):$BiVO_4$ photoanodes. (e) Mott−Schottky analysis in KPi electrolyte measured in the dark (inset: the shift in the CB edge) for photoanodes with WO_3 heterojunction and Bi_2O_3 interface layer with and without sulfur modification. (f) photocurrent onset measurement in KPi under Simulated AM 1.5G illumination. Frequency-dependent relationship of (g) real and (h) imaginary impedance.

Section 5: Absorption, charge separation and transport

Figure S5c shows charge separation (ϕ_{sep}) and hole transfer efficiencies (ϕ_{trans}), where it is seen that the Ga doped sample demonstrated better ϕ_{sep} (38%) compared to i-$BiVO_4$ (26%), likely due to improved conductivity and increased charge carrier concentration (Table S1). Likewise, the co-doped sample (Ga,W):$BiVO_4$ exhibited better charge separation (66%) compared to W:$BiVO_4$ (62%). This is possibly due to the cumulative effect of W and Ga where Ga acts as an electron donor, forming a diffusion path that reduces recombination of photogenerated charge carriers.[2,9] Correspondingly, ϕ_{trans} in Figure S5d follows a similar trend to that of ϕ_{sep} where (Ga,W):$BiVO_4$ samples exhibit the highest charge transfer rate (51%) compared to W:$BiVO_4$ (35%), Ga:$BiVO_4$ (16%) and $BiVO_4$ (8.4%) samples. The calculated ϕ_{sep} and ϕ_{trans} for the heterojunction based sample WO_3/S:Bi_2O_3/(Ga,W):$BiVO_4$ (Figure S5e and f) demonstrated the highest ϕ_{sep} (95%) compared to WO_3/Bi_2O_3/(Ga,W):$BiVO_4$ (89%) and WO_3/(Ga,W):$BiVO_4$ (87%). Correspondingly, the obtained ϕ_{trans} for WO_3/S:Bi_2O_3/(Ga,W):$BiVO_4$ photoanode was highest ϕ_{trans} (80%) compared to WO_3/Bi_2O_3/(Ga,W):$BiVO_4$ (65%) and WO_3/(Ga,W):$BiVO_4$ (53%). This validates that using the S:Bi_2O_3 interfacial layer can facilitate photogenerated charge separation and act as a blocking layer for holes generated in $BiVO_4$ absorber layer. In this case, electrons generated in the $BiVO_4$ can rapidly transport to the charge collector which reduces the probability of electrons becoming trapped at recombination sites. In parallel, holes can readily transfer to the reaction surface for water splitting.

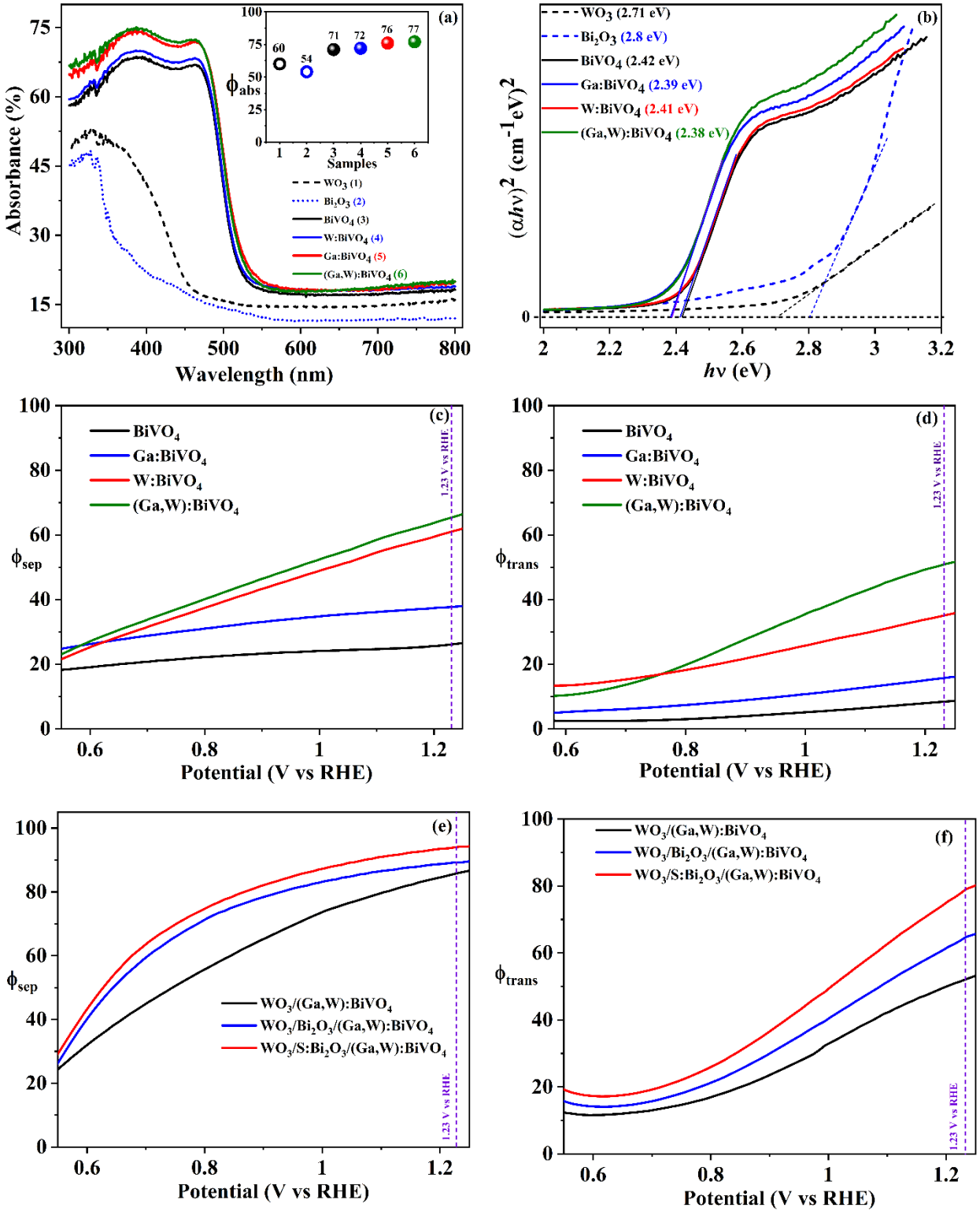

Figure S5. *(a) Absorption spectra (inset: absorption efficiency), (b) bandgap, (c) charge separation efficiency (ϕ_{sep}) and (d) charge transfer efficiency (ϕ_{trans}) for all doped photoanodes. (e) charge separation efficiency (ϕ_{sep}) and (f) charge transfer efficiency (ϕ_{trans}) for photoanodes with WO_3 heterojunction and Bi_2O_3 interface layer with and without sulfur modification.*

Section 6: Scanning electron microscopy of $BiVO_4$, WO_3, Bi_2O_3 and FTO substrate

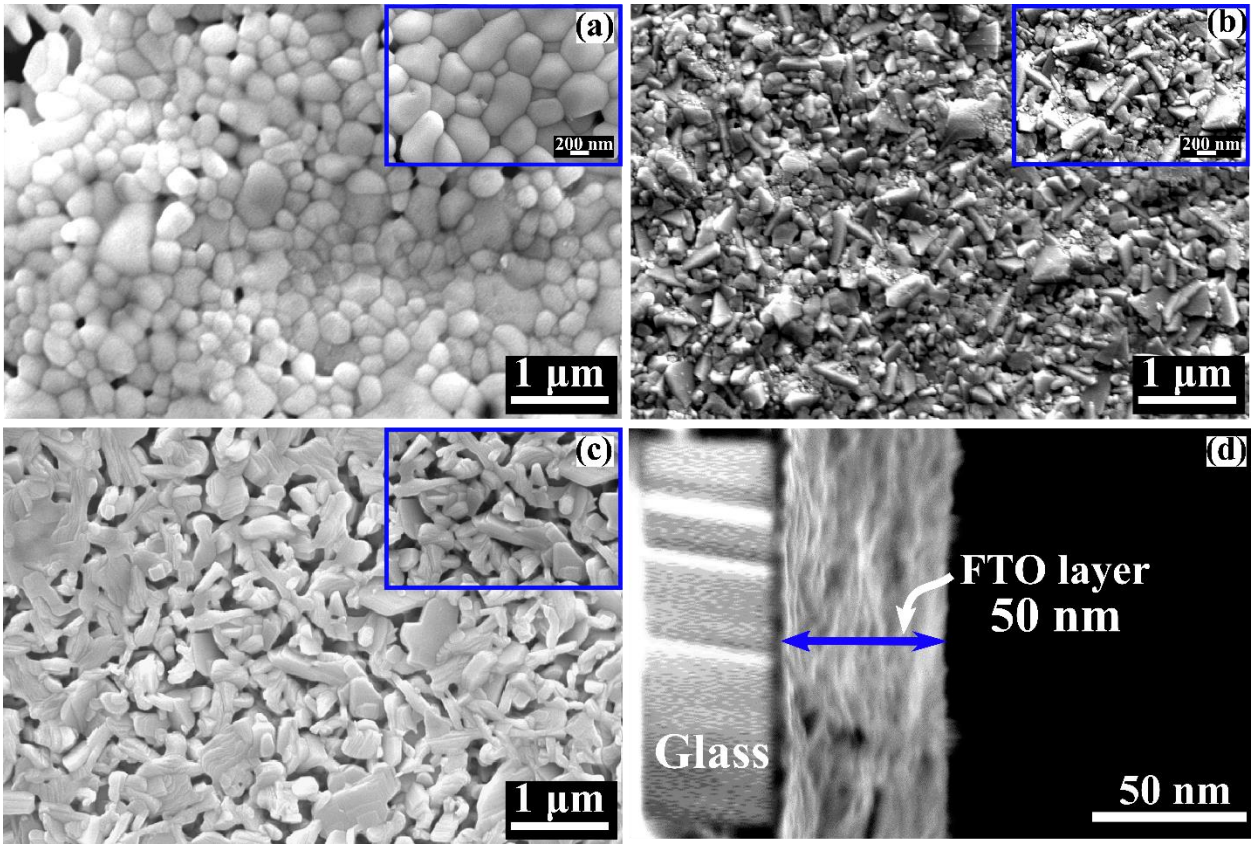

Figure S6. Surface morphology of (a) i-$BiVO_4$, (b) WO_3, (c) Bi_2O_3. (d) Cross-sectional image of FTO coating on the glass substrate.

Section 7: XRD

The phase identification, purity and crystal structure of all fabricated thin films were examined using XRD (PANalytical X'Pert PRO MRD; Cu Kα radiation; 0.006 degrees per sec). The crystal structure was determined using XRD analysis for intrinsic and doped $BiVO_4$, Bi_2O_3 and WO_3 in Figure S7a. It was noticed that all characteristic peaks of $BiVO_4$ were matched with standard PDF #014-0688 and confirmed the clinobisvanite (monoclinic scheelite) structure. However, there were no doping-oriented peaks identified after 4 wt% Ga and 1.3 wt% W doping in $BiVO_4$, which validated that doping did not make any changes in the crystal structure/space group of $BiVO_4$.

Bi_2O_3 was identified to have a tetragonal phase with standard PDF # 18-0244 whereas WO_3 had a monoclinic form with standard PDF # 43-1035. In the next step, XRD analysis was conducted for heterojunction samples in Figure S7b. The individual peaks of WO_3, Bi_2O_3 and $BiVO_4$ were identified and confirmed the successful formation of a heterojunction without any complex phases. There were no S oriented peaks identified, possibly due to the small amount of S in the film WO_3/S:Bi_2O_3/(Ga,W):$BiVO_4$.

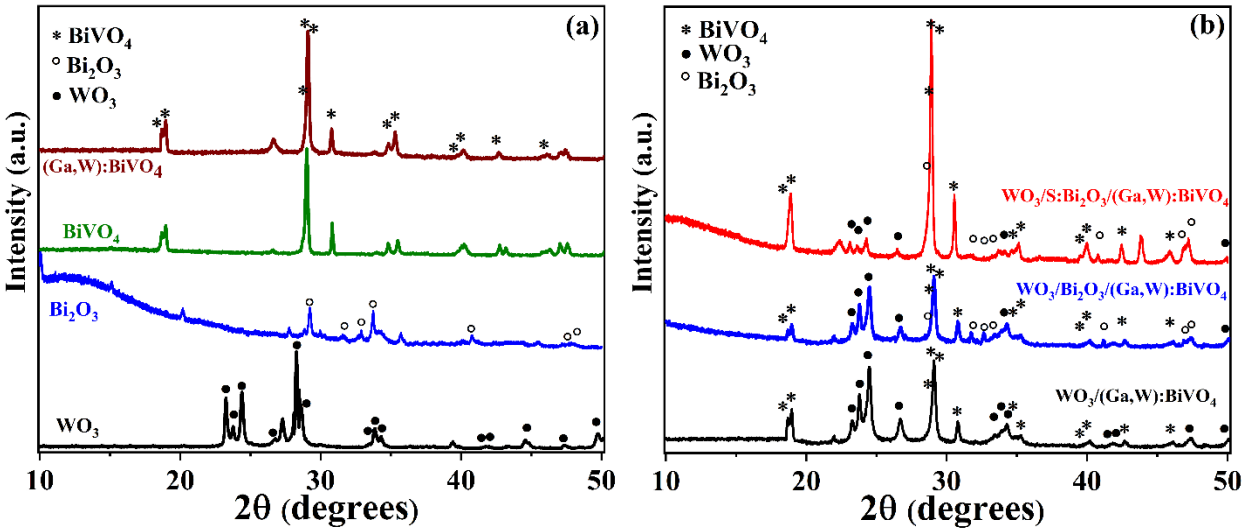

Figure S7. XRD analysis of (a) WO_3, Bi_2O_3, $BiVO_4$ and (Ga,W):$BiVO_4$ and (b) photoanodes with WO_3 heterojunction and Bi_2O_3 interface layer with and without sulfur modification.

Section 8: XPS

XPS was employed to determine the oxidation state of Bi, V, W, Ga and O in the WO_3/S:Bi_2O_3/(Ga,W):$BiVO_4$ sample. From Figures S8a-e, the major peaks for Bi $4d_{3/2}$ (467.5 eV), Bi $4d_{5/2}$ (443.8 eV), Bi $4f_{5/2}$ (167.7 eV), Bi $4f_{7/2}$ (159.4 eV), V $2p_{1/2}$ (524.4 eV), V $2p_{3/2}$ (516.9 eV), W $4f_{5/2}$ (38.9 eV), W $4f_{1/2}$ (35.9 eV), Ga $2p_{1/2}$ (1144.7 eV), Ga $2p_{3/2}$ (1118 eV) were observed and attributed the oxidation states as +3 and +5, +6 and +3 for Bi, V, W and Ga, respectively. XPS spectra in the O 1s in Figure S8f illustrates the nominal oxidation state of O (-2) with lattice oxygen (V−O) at 530 eV, and the shoulder at 531 eV confirmed the surface-adsorbed oxygen (−OH). No

extra peaks due to Ga doping were observed, which confirmed that Ga^{3+} doping at Bi^{3+} sites was successful.

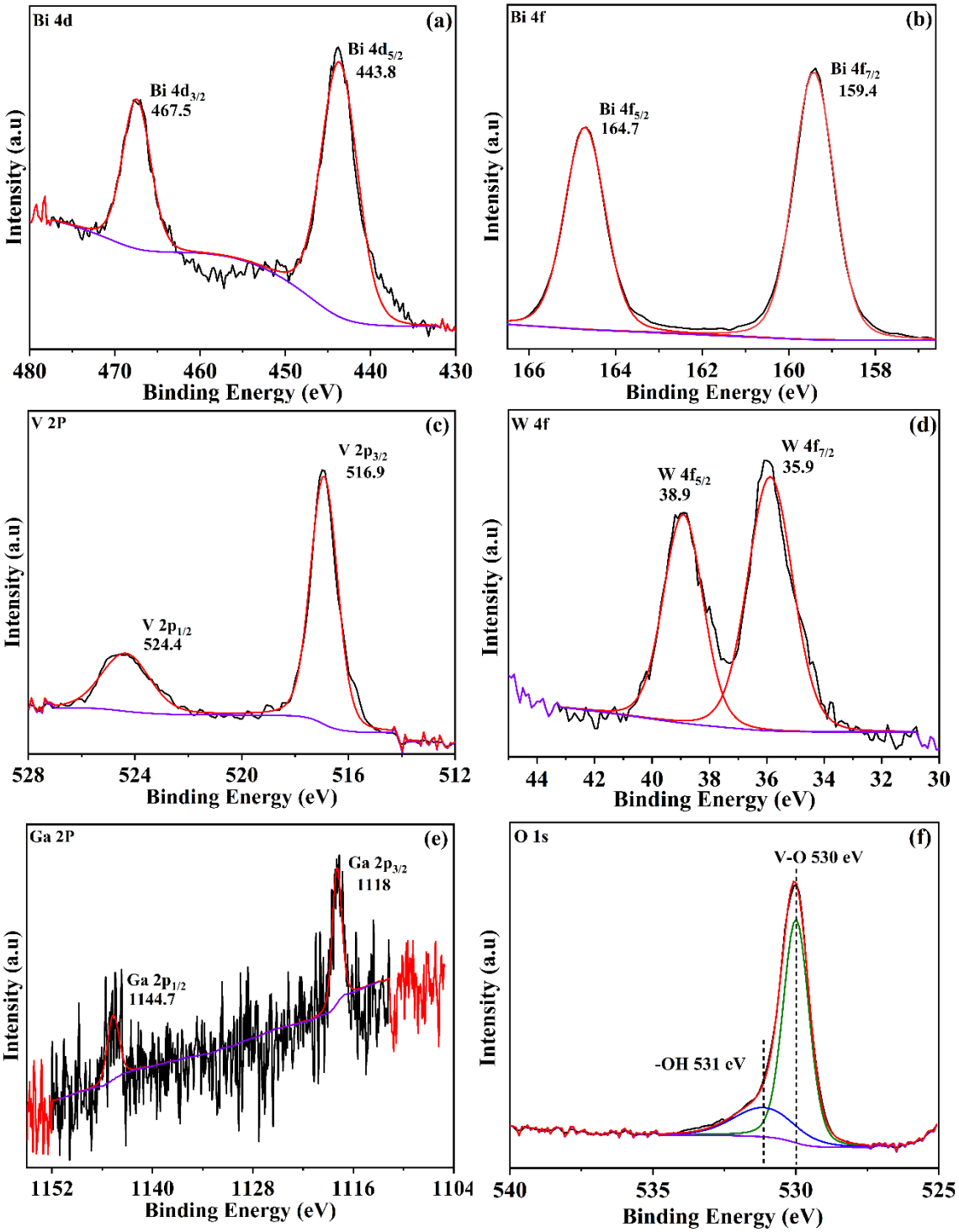

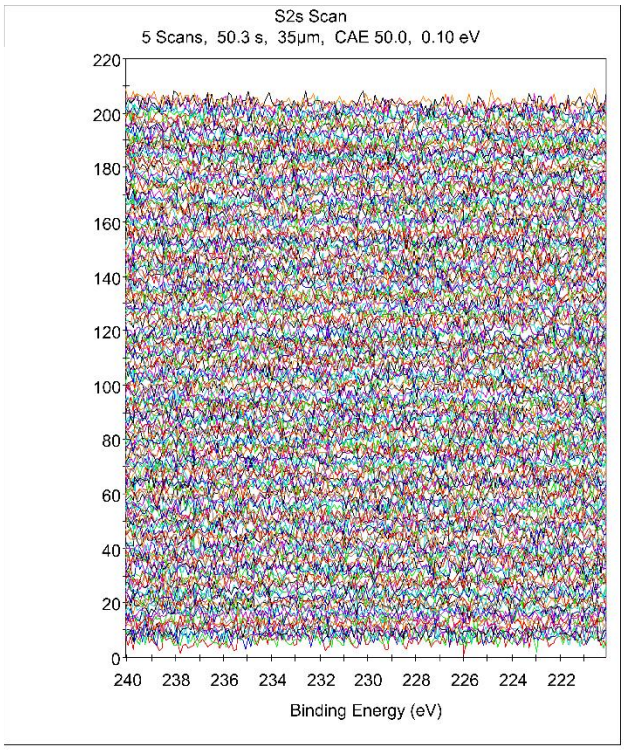

(g)

(h)

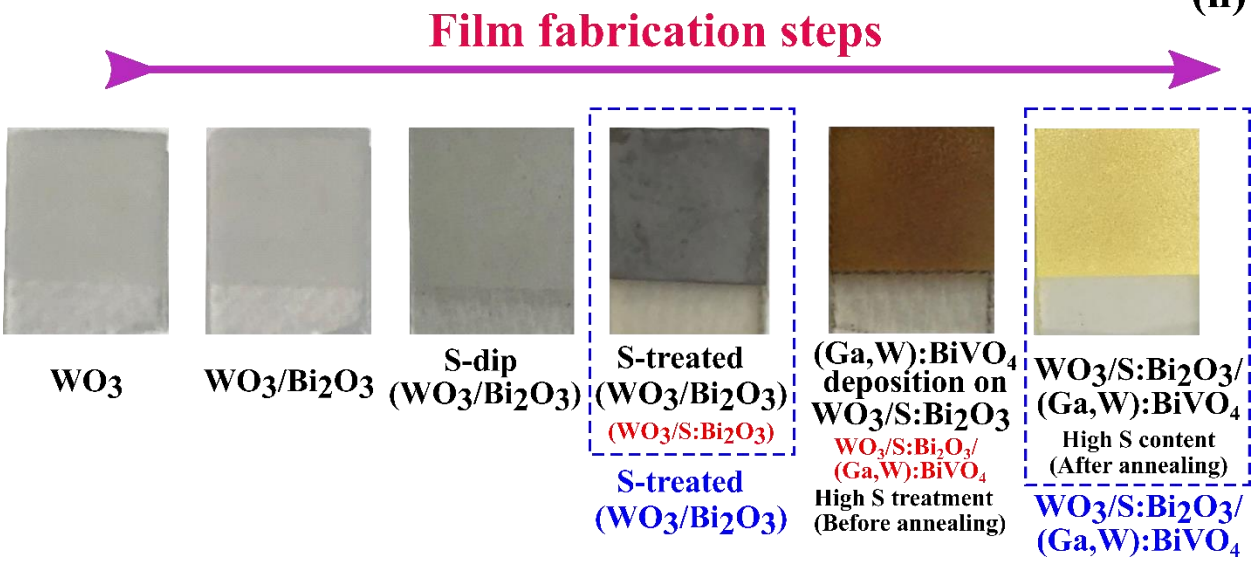

Figure S8. XPS surface spectra of (a) Bi 4d, (b) Bi 4f, (d)V 2p, (e)W 4f, (f) Ga 2p and (g) O 1s. (g) XPS depth profiling spectra for S 2s. (h) Prepared samples for the XPS surface analysis to determine the state of sulfur.

Section 9: TOF-SIMS depth profiling

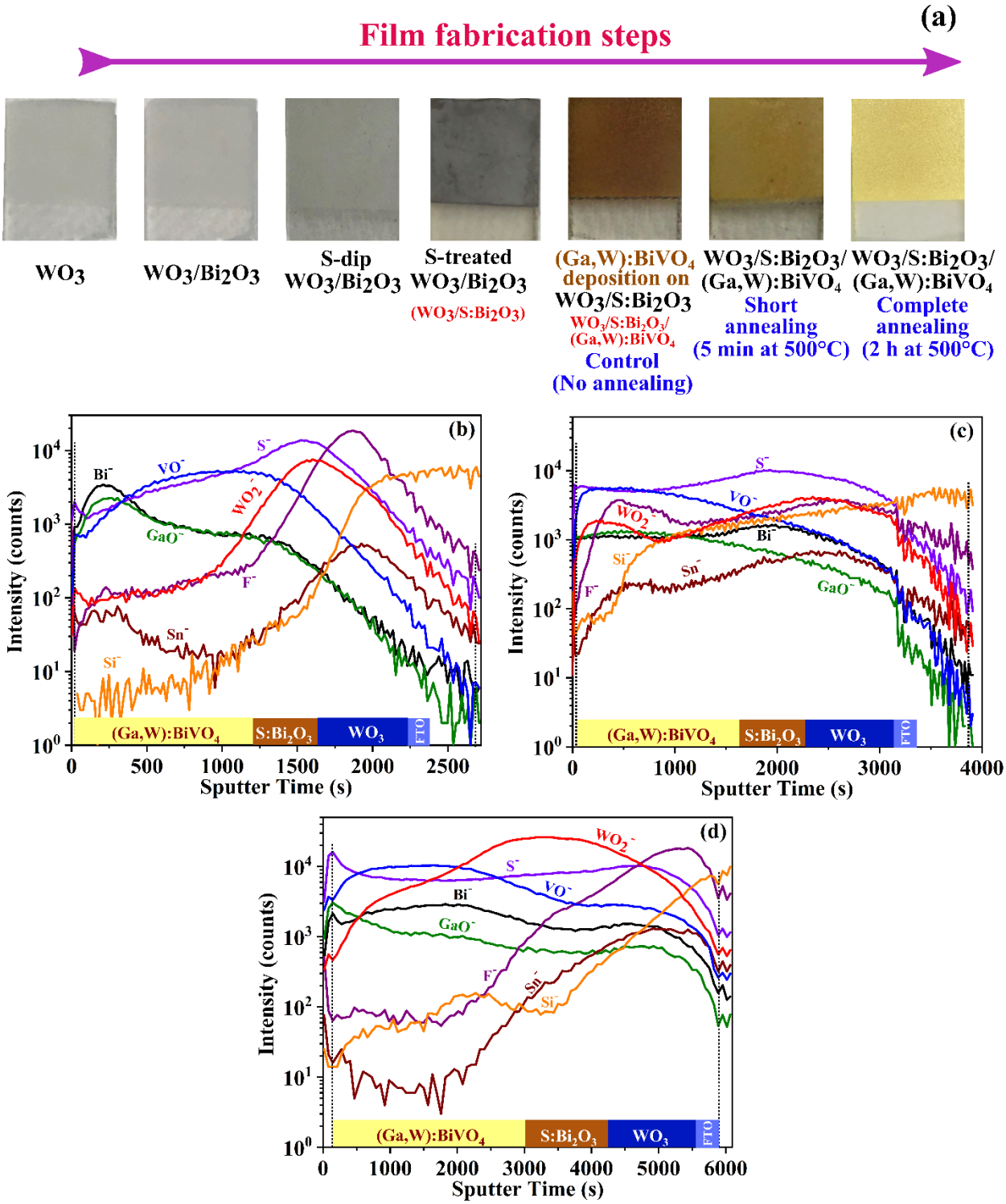

Figure S9. (a) Process of prepared samples for depth profiling in three distinct environments. Negative polarity time of flight secondary ion mass spectroscopy (TOF-SIMS) analysis of sample $WO_3/S:Bi_2O_3/(Ga,W):BiVO_4$ in three distinct environments (b) control (no annealing), (c) short annealing (5 min at 500°C) and (d) complete annealing (2h at 500°C) for Bi^-, VO^-, WO^{2-}, GaO^-,

S^-, F^-, Sn^- and Si^-species. Note the substrate signals appear midway through the film due to the poor depth resolution of the profiles, owing to the roughness of the films at the start of profiling

Section 10: Randles circuits and reproducibility validation

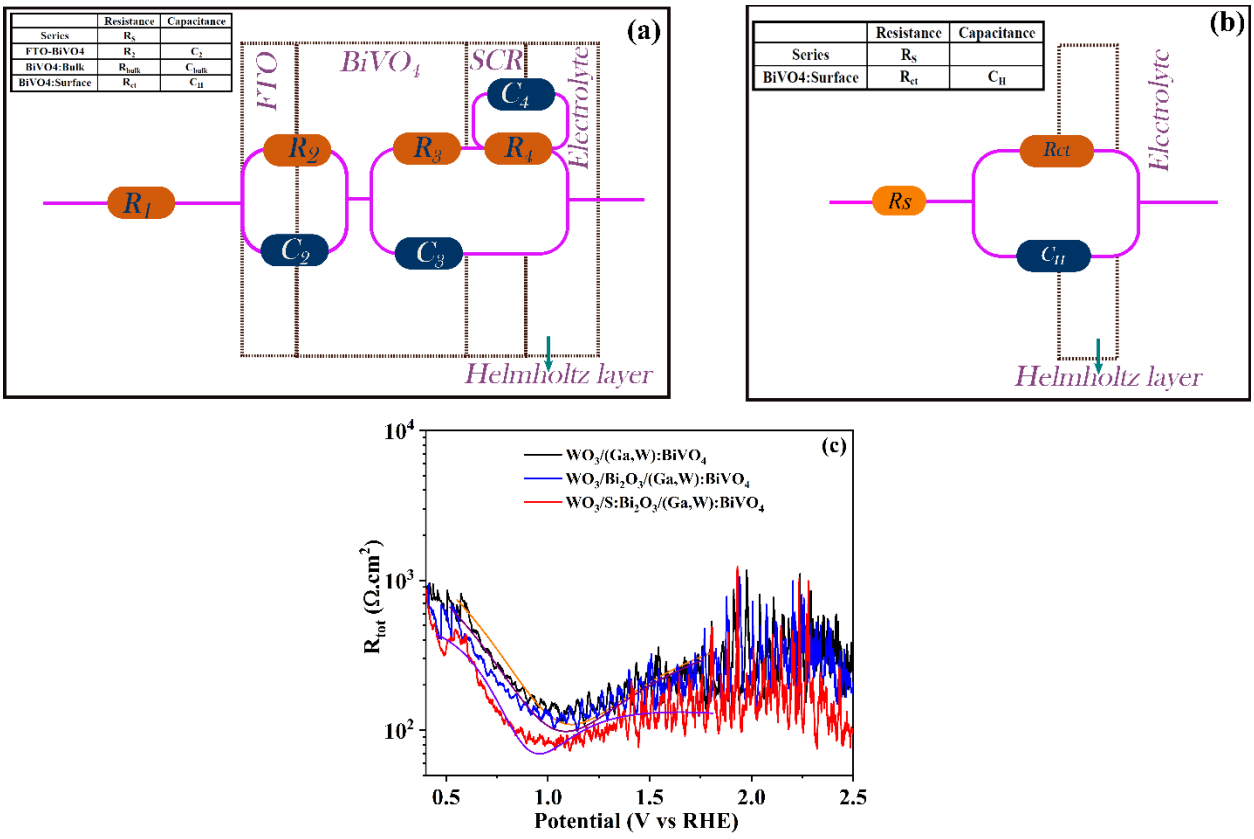

Figure S10. (a) and (b) Randles circuit for calculating $R_{surface}$, R_{bulk}, $C_{surface}$ and C_{bulk}. (c) R_{tot} calculated by $(\frac{dI}{dV})^{-1}$ and fitting was done using GaussMod function in OriginPro 2020.

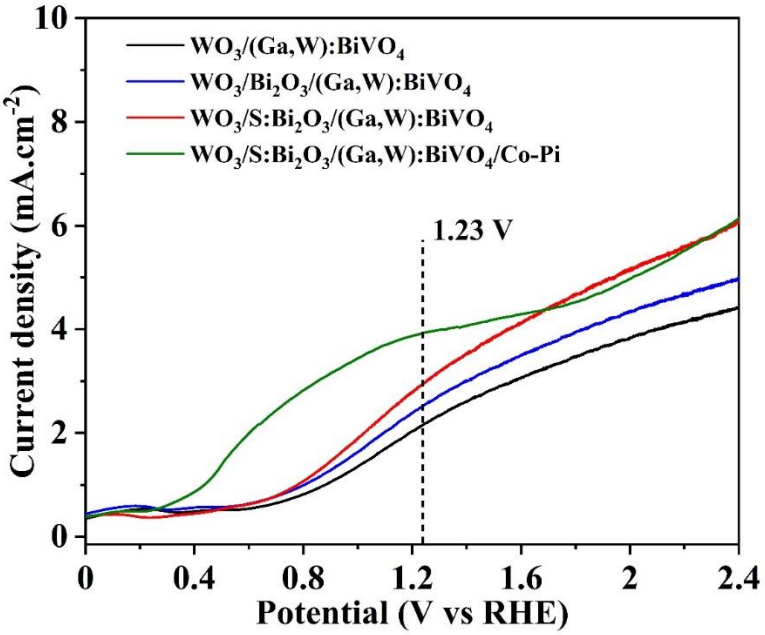

Figure S11. J-V plot after stability measurement for reproducibility validation of photoanodes with WO_3 heterojunction and Bi_2O_3 interface layer with and without sulfur modification.

Tables

Table S1: Result summary: WO3, Bi2O3, intrinsic and modified $BiVO_4$

Photoanode	PCD ($mA.cm^{-2}$)	Band Gap (eV)	Current onset (V)	Flat band Potential (V)	Charge carrier density (cm^{-3})	
WO_3		2.71				
Bi_2O_3		2.8				
i-$BiVO_4$	0.25±0.01	2.42	0.23	0.25	2.8916E+19	
Ga:$BiVO_4$	0.4±0.02	2.39	0.18	0.21	9.62267E+19	
W:$BiVO_4$	1.02±0.04	2.41	0.11	0.18	1.04236E+20	
(Ga,W):$BiVO_4$	1.68±0.1	2.38	0.07	0.15	1.04236E+20	

Table S1b: Result summary: heterojunction samples, Bi_2O_3 layer without and with sulfur.

Photoanode	PCD ($mA.cm^{-2}$)	PCD in Hole scavanger ($mA.cm^{-2}$)	Current onset (V)	Flat band Potential (V)	Charge carrier density (cm^{-3})	IPCE (%)
WO_3/(Ga,W):$BiVO_4$	2.8±0.12	5.4±0.26	-0.15	0.092	1.14522E+20	43.2
WO_3/Bi_2O_3/(Ga,W):$BiVO_4$	3.27±0.15	5.86±0.28	-0.18	0.048	1.26141E+20	53.5
WO3/S:Bi_2O_3/(Ga,W):$BiVO_4$	4±0.2	6.4±0.3	-0.21	0.041	1.80388E+20	63.25
WO3/S:Bi_2O_3/(Ga,W):$BiVO_4$/Co-Pi	5.1±0.25					73.5

Table S2: Time-resolved PL analysis calculated parameters

Photoanode	A_1	τ_1 (ns)	A_2	τ_2 (ns)	$<\tau>$ (ns)	K_{et}(ns^{-1})
WO_3/(Ga,W):$BiVO_4$	646.31±81.42	0.34±0.03	23.88±8.94	1.39±0.24	0.477±0.05	2.095±0.20
WO_3/S:Bi_2O_3/(Ga,W):$BiVO_4$	679.97±90.52	0.31±0.03	37.54±17.41	1.02±0.18	0.418±0.04	2.393±0.22

Table S3: fs-TA analysis calculated parameters of dry film

	WO_3/(Ga,W):$BiVO_4$		WO_3/S:Bi_2O_3/(Ga,W):$BiVO_4$	
	A	τ (ps)	A	τ (ps)
τ_1	1.06E-02	1.164	1.95E-03	1.947
τ_2	5.50E-03	31.15	1.45E-03	60.45
τ_3	2.96E-03	4640	1.35E-03	8233

Table S4: ns-TA analysis calculated parameters in operando

	WO_3/(Ga,W):$BiVO_4$			WO_3/S:Bi_2O_3/(Ga,W):$BiVO_4$		
	A	τ (ns)	K_{TA} (ns^{-1})	A	τ (ns)	K_{TA} (ns^{-1})
τ_1	0.43	2.5	0.4	0.35	1.1	0.909

τ_2	0.38	43	0.023	0.37	36	0.0278
τ_3	0.21	1300	0.0008	0.21	1100	0.0009
τ_4	0.07	>100000	<0.00001	0.07	>100000	<0.00001

Table S5: Comparison of improved photocurrent density in $WO_3/BiVO_4$ heterojunction with various interfacial layers.

	Photoanode	**Electrolyte**	**Photocurrent ($mA.cm^{-2}$)**	**Month**	**Year**	**Ref**
1	FTO/WO_3/$BiVO_4$/Au	0.5 M Na_2SO_4	0.072	January	2010	[10]
2	$BiVO_4$/SnO_2/WO_3	0.1 M Na_2SO_4	2.7	March	2012	[11]
3	$BiVO_4$/WO_3/W	0.1 M KH_2PO_4	2.01	October	2015	[12]
4	WO_3/$BiVO_4$/TiO_2 core–shell	0.1 M Na_2SO_4	4.2	October	2016	[13]
5	$BiVO_4$/WO_3/SnO_2	Phosphate buffer	3.1	December	2016	[14]
6	WO_3/W:$BiVO_4$/$BiVO_4$	0.5 M Na_2SO_4	2.74	January	2017	[15]
7	$BiVO_4$/(RGO/WO_3)/$W_{18}O_{49}$/FeOOH/NiOOH	0.5 M Na_2SO_4	2.4	January	2018	[16]
8	FTO–$BiVO_4$–W–WO_3	0.1 M Na_2SO_4	2.7	June	2018	[17]
9	Al2O3/$BiVO_4$/WO_3	2.0 M $KHCO_3$	4	June	2018	[18]
10	FeOOH/Au-surface/$BiVO_4$/WO_3/Au-bottom	0.5 M Na_2SO_4	1.97	December	2018	[19]
11	WO3/BiVO4/ZnO	0.5 M Na_2SO_4	2.96	December	2018	[20]
12	TiO_2/BiVO4/SnO_2	0.5 M phosphate buffer	2.3	January	2019	[21]
13	3D TiO_2/WO_3/$BiVO_4$/FeOOH/NiOOH TiO2/WO3/BiVO4/FeOOH/NiOOH	0.5 M Na_2SO_4	4.27	June	2019	[22]
14	WO_3/$BiVO_4$/BiOCl	0.1 M Na_2SO_4	0.00724	June	2019	[23]
15	FTO|WO3/CuWO4|$BiVO_4$	0.1 M phosphate buffer	0.66	April	2019	[24]
16	WO_3/$BiVO_4$ (BVO)/$BiFeO_3$	0.5 mol·L^{-1} Na_2SO_4	1.5	August	2019	[25]
17	WO_3-TiO_2-$BiVO_4$	0.1M Na_2S+0.2M NaOH	0.03	November	2019	[26]
18	CNP/B-$BiVO_4$/WO_3	0.1 M Na_2SO_4	0.44	March	2020	[27]
19	WO_3/$BiVO_4$_Bi-PED	Na_2SO_4 0.5 mol L^{-1} + Na_2HPO_4 0.1 mol L^{-1} pH 7.0	2.1 ± 0.3	June	2020	[28]

20	$WO_3/BiVO_4$/TANiFe	Borate buffer	3.7	July	2020	[29]
21	WO_3/S:Bi_2O_3/(Ga,W):$BiVO_4$	0.1 M K_2HPO_4	4		2021	This work
22	WO_3/S:Bi_2O_3/(Ga,W):$BiVO_4$/Co-Pi	0.1 M K_2HPO_4	5.14		2021	This work

Table S6: Comparison of hydrogen generation rate for $BiVO_4$ based heterojunction.

	Photoanode	Electrolyte	Gas collection rate ($\mu mol\ h^{-1}cm^{-2}$)		Month	Year	Ref
			H_2	O_2			
1	$BiVO_4$/FeOOH/NiOOH	0.5 M Na_2SO_4	3.5	1.84	February	2014	[30]
2	WO_3-NRs/$BiVO_4$+CoPi	0.5 M Na_2SO_4	47.8	23.6	May	2014	[31]
3	WO_3/(W, Mo)-$BiVO_4$/FeOOH/NiOOH	0.5M K2SO4	94.23	46.32	September	2014	[32]
4	WO3-NRs/BiVO4+CoPi	pH 7	102	58	June	2015	[33]
5	TiO_2@$BiVO_4$	0.1 M phosphate buffered saline (PBS)	16.17		September	2015	[34]
6	3 wt% RuO_2/$GBVO_{0.10}$	pH 7	48.7	25	October	2015	[35]
7	CDs/$BiVO_4$ QDs	0.5M phosphate buffer	0.92	0.51	August	2016	[36]
8	$WO_3/BiVO_4/TiO_2$	0.1 M Na_2SO_4	25.6		October	2016	[13]
9	HDP($BiVO_4$||Fe_2O_3)	1.0M KCl	100	54.5	December	2016	[37]
10	$SrTiO_3$:La,Rh/C/$BiVO_4$:Mo	0.1 M Na_2SO_4	16.67	8.34	January	2017	[38]
11	$BiVO_4$-SnO_2-15/Pt	0.2 M sodium borate	1.16		April	2017	[39]
12	FeOOH/NiOOH + $BiVO_4$/(RGO/WO_3)/$W_{18}O_{49}$	0.5 M Na_2SO_4	3.14	5.24	January	2018	[16]
13	$FeCoO_x/BiVO_4$	1M potassium borate	86	42	June	2018	[40]
14	CoPi/$NiMoO_4$/$BiVO_4$	0.5 M Na_2SO_4	94.65	46.7	June	2018	[41]
15	$BiVO_4$ @Co-MIm	0.5 M Na_2SO_4	53.67	26.34	April	2019	[42]
16	CoS/$BiVO_4$	0.5 M Na_2SO_4	51.9	25.7	April	2019	[43]
17	WO_3/g-C_3N_4	0.04M Na2SO3 & 0.1 M Na2S	72.5		May	2019	[44]
18	b-$BiVO_4/TiO_2$−x	0.5M potassium phosphate	49.67	25.64	June	2019	[45]

		buffered with 1 m Na2SO3					
19	$BiVO_4/CTP_2$	0.1 M phosphate buffer	67.6	33.8	October	2019	[46]
20	Fe_2O_3/ $BiVO_4$10	0.5 M Na_2SO_4	46.34		November	2019	[47]
21	BVO/MoS_x(Nafion)−PV4	phosphate-buffered solution (PBS)	28.6	14.08	March	2020	[48]
22	$BiVO_4$/NiFeOOH/Co-Pi	0.5 M Na_2SO_4	7	3.6	March	2020	[49]
23	WO_3-ZIF-67/$BiVO_4$-BP	0.5 M Na_2SO_4	15.9	7.85	May	2020	[50]
24	0.8wt % g-C_3N_4/$BiVO_4$	0.5 M Na_2SO_4	21.4		June	2020	[51]
25	$BiVO_4$/Ov/FeOx	KPi	48.2	23.8	July	2020	[52]
26	$ZnIn_2S_4/BiVO_4$	0.1 M Na_2SO_4	62.44		August	2020	[53]
27	Cu_2O/Pt/$BiVO_4$	10% methanol	1.7		December	2020	[54]
28	WO_3/S:Bi_2O_3/(Ga,W):$BiVO_4$/Co-Pi	0.1M K2HPO4	67.3	33.6	This work		

References:

1 U. Prasad, J. Prakash and A. M. Kannan, *Sustain. Energy Fuels*, 2020, **4**, 1496–1506.

2 U. Prasad, J. Prakash, S. K. Gupta, J. Zuniga, Y. Mao, B. Azeredo and A. N. M. Kannan, *ACS Appl. Mater. Interfaces*, 2019, **11**, 19029–19039.

3 U. Prasad, J. Prakash, X. Shi, S. K. Sharma, X. Peng and A. M. Kannan, *ACS Appl. Mater. Interfaces*, 2020, **12**, 52808-5281.

4 B. C. Xiao, L. Y. Lin, J. Y. Hong, H. S. Lin and Y. T. Song, *RSC Adv.*, 2017, **7**, 7547–7554.

5 J. Resasco, H. Zhang, N. Kornienko, N. Becknell, H. Lee, J. Guo, A. L. Briseno and P. Yang, *ACS Cent. Sci.*, 2016, **2**, 80–88.

6 U. Prasad, J. Prakash, B. Azeredo and A. Kannan, *Electrochim. Acta*, 2019, **299**, 262–272.

7 C. Liu, J. Su and L. Guo, *RSC Adv.*, 2016, **6**, 27557–27565.

8 Z. Chen, H. N. Dinh and E. Miller, *Photoelectrochemical Water Splitting*, 2013.

9 K. Pal, S. Parmar, J. Kang, A. Bist, P. Dua and S. Jang, 2012, **784**, 1926–1934.

10 P. Chatchai, S. ya Kishioka, Y. Murakami, A. Y. Nosaka and Y. Nosaka, *Electrochim. Acta*, 2010, **55**, 592–596.

11 R. Saito, Y. Miseki and K. Sayama, *Chem. Commun.*, 2012, **48**, 3833–3835.

12 L. Xia, J. Bai, J. Li, Q. Zeng, X. Li and B. Zhou, *Appl. Catal. B Environ.*, 2016, **183**, 224–

230.

13 S. S. Kalanur, I. H. Yoo, J. Park and H. Seo, *J. Mater. Chem. A*, 2017, **5**, 1455–1461.

14 J. H. Baek, B. J. Kim, G. S. Han, S. W. Hwang, D. R. Kim, I. S. Cho and H. S. Jung, *ACS Appl. Mater. Interfaces*, 2017, **9**, 1479–1487.

15 J. Choi, P. Sudhagar, J. H. Kim, J. Kwon, J. Kim, C. Terashima, A. Fujishima, T. Song and U. Paik, *Phys. Chem. Chem. Phys.*, 2017, **19**, 4648–4655.

16 Z. Zhang, B. Chen, M. Baek and K. Yong, *ACS Appl. Mater. Interfaces*, 2018, **10**, 6218–6227.

17 R. Wang, T. Xie, T. Zhang, T. Pu, Y. Bu and J. P. Ao, *J. Mater. Chem. A*, 2018, **6**, 12956–12961.

18 Y. Miyase, S. Takasugi, S. Iguchi, Y. Miseki, T. Gunji, K. Sasaki, E. Fujita and K. Sayama, *Sustain. Energy Fuels*, 2018, **2**, 1621–1629.

19 B. Chen, Z. Zhang, M. Baek, S. Kim, W. Kim and K. Yong, *Appl. Catal. B Environ.*, 2018, **237**, 763–771.

20 Z. Ma, K. Song, L. Wang, F. Gao, B. Tang, H. Hou and W. Yang, *ACS Appl. Mater. Interfaces*, 2019, **11**, 889–897.

21 S. W. Hwang, J. U. Kim, J. H. Baek, S. S. Kalanur, H. S. Jung, H. Seo and I. S. Cho, *J. Alloys Compd.*, 2019, **785**, 1245–1252.

22 Q. Pan, H. Zhang, Y. Yang and C. Cheng, *Small*, 2019, **15**, 1–9.

23 H. Li, Y. Chen, W. Zhou, H. Jiang, H. Liu, X. Chen and T. Guohui, *J. Alloys Compd.*, 2019, **802**, 76–85.

24 I. Rodríguez-Gutiérrez, E. Djatoubai, M. Rodríguez-Pérez, J. Su, G. Rodríguez-Gattorno, L. Vayssieres and G. Oskam, *Electrochim. Acta*, 2019, **308**, 317–327.

25 S. Khoomortezaei, H. Abdizadeh and M. R. Golobostanfard, *ACS Appl. Energy Mater.*, 2019, **2**, 6428–6439.

26 Y. Yang and Y. F. Cheng, *Corros. Sci.*, 2020, **164**, 108333.

27 G. M. Peleyeju, E. H. Umukoro, J. O. Babalola and O. A. Arotiba, *ACS Omega*, 2020, **5**, 4743–4750.

28 D. Coelho, J. P. R. S. Gaudêncio, S. A. Carminati, F. W. P. Ribeiro, A. F. Nogueira and L. H. Mascaro, *Chem. Eng. J.*, 2020, **399**, 125836.

29 H. Sun, W. Hua, Y. Li and J. G. Wang, *ACS Sustain. Chem. Eng.*, 2020, **8**, 12637–12645.

30 T. W. Kim and K.-S. Choi, *Science (80-.).*, 2014, **343**, 990 LP – 994.

31 Y. Pihosh, I. Turkevych, K. Mawatari, T. Asai, T. Hisatomi, J. Uemura, M. Tosa, K. Shimamura, J. Kubota, K. Domen and T. Kitamori, *Small*, 2014, **10**, 3692–3699.

32 X. Shi, I. Y. Choi, K. Zhang, J. Kwon, D. Y. Kim, J. K. Lee, S. H. Oh, J. K. Kim and J. H.

Park, *Nat. Commun.*, 2014, **5**, 1–8.

33 Y. Pihosh, I. Turkevych, K. Mawatari, J. Uemura, Y. Kazoe, S. Kosar, K. Makita, T. Sugaya, T. Matsui, D. Fujita, M. Tosa, M. Kondo and T. Kitamori, *Sci. Rep.*, 2015, **5**, 1–2.

34 X. Zhang, B. Zhang, K. Cao, J. Brillet, J. Chen, M. Wang and Y. Shen, *J. Mater. Chem. A*, 2015, **3**, 21630–21636.

35 W. J. Jo, H. J. Kang, K. J. Kong, Y. S. Lee, H. Park, Y. Lee, T. Buonassisi, K. K. Gleason and J. S. Lee, *Proc. Natl. Acad. Sci. U. S. A.*, 2015, **112**, 13774–13778.

36 X. Wu, J. Zhao, S. Guo, L. Wang, W. Shi, H. Huang, Y. Liu and Z. Kang, *Nanoscale*, 2016, **8**, 17314–17321.

37 J. H. Kim, J. W. Jang, Y. H. Jo, F. F. Abdi, Y. H. Lee, R. Van De Krol and J. S. Lee, *Nat. Commun.*, 2016, **7**, 1–9.

38 Q. Wang, T. Hisatomi, Y. Suzuki, Z. Pan, J. Seo, M. Katayama, T. Minegishi, H. Nishiyama, T. Takata, K. Seki, A. Kudo, T. Yamada and K. Domen, *J. Am. Chem. Soc.*, 2017, **139**, 1675–1683.

39 M. Xie, Z. Zhang, W. Han, X. Cheng, X. Li and E. Xie, *J. Mater. Chem. A*, 2017, **5**, 10338–10346.

40 S. Wang, T. He, J. H. Yun, Y. Hu, M. Xiao, A. Du and L. Wang, *Adv. Funct. Mater.*, 2018, **28**, 1–10.

41 L. Gao, F. Li, H. Hu, X. Long, N. Xu, Y. Hu, S. Wei, C. Wang, J. Ma and J. Jin, *ChemSusChem*, 2018, **11**, 2502–2509.

42 S. Zhou, P. Yue, J. Huang, L. Wang, H. She and Q. Wang, *Chem. Eng. J.*, 2019, **371**, 885–892.

43 H. She, M. Jiang, P. Yue, J. Huang, L. Wang, J. Li, G. Zhu and Q. Wang, *J. Colloid Interface Sci.*, 2019, **549**, 80–88.

44 M. Bilal Tahir, K. Nadeem Riaz and A. M. Asiri, *Int. J. Energy Res.*, 2019, **43**, 5747–5758.

45 Z. Tian, P. Zhang, P. Qin, D. Sun, S. Zhang, X. Guo, W. Zhao, D. Zhao and F. Huang, *Adv. Energy Mater.*, 2019, **9**, 1901287.

46 Q. Pan, T. Chen, L. Ma, G. Wang, W. B. Hu, Z. Zou, K. Wen and H. Yang, *Chem. Mater.*, 2019, **31**, 8062–8068.

47 Y. lei Li, Y. Liu, Y. juan Hao, X. jing Wang, R. hong Liu and F. tang Li, *Mater. Des.*, 2020, **187**, 108379.

48 S. Zhang, L. Shen, T. Ye, K. Kong, H. Ye, H. Ding, Y. Hu and J. Hua, *Energy & Fuels*, 2020, **34**, 5016–5023.

49 G. Fang, Z. Liu and C. Han, *Appl. Surf. Sci.*, 2020, **515**, 146095.

50 Y. Wang, H. Shi, K. Cui, L. Zhang, S. Ge and J. Yu, *Appl. Catal. B Environ.*, 2020, **275**, 119094.

51 M. F. R. Samsudin, H. Ullah, R. Bashiri, N. M. Mohamed, S. Sufian and Y. H. Ng, *ACS Sustain. Chem. Eng.*, 2020, **8**, 9393–9403.

52 Y. Zhang, J. Bai, J. Wang, S. Chen, H. Zhu, J. Li, L. Li, T. Zhou and B. Zhou, *Chem. Eng. J.*, 2020, **401**, 126134.

53 J. Hu, C. Chen, Y. Zheng, G. Zhang, C. Guo and C. M. Li, *Small*, 2020, 16.

54 J. Liu, B. Zhang, Y. Xiang and G. Ma, *New J. Chem.***,** 2021,**45**, 517-521.